HAL open science

Highly crystalline hexagonal PbI2 sheets on polyaniline/antimony tin oxide surface as a novel and highly efficient photodetector in UV, Vis, and near IR regions

Nomery Hadia, Mohamed Shaban, S. Mohamed, Ali Al-Ghamdi, Meshal Alzaid, Asmaa Elsayed, Abdel Hamid I. Mourad, Mohammed Amin, Rabah Boukherroub, Ahmed Adel A. Abdelazeez, et al.

To cite this version:

Nomery Hadia, Mohamed Shaban, S. Mohamed, Ali Al-Ghamdi, Meshal Alzaid, et al.. Highly crystalline hexagonal PbI2 sheets on polyaniline/antimony tin oxide surface as a novel and highly efficient photodetector in UV, Vis, and near IR regions. Polymers for Advanced Technologies, 2022, 33 (12), pp.3977-3987. 10.1002/pat.5829 . hal-03770752

HAL Id: hal-03770752

https://hal.science/hal-03770752v1

Submitted on 12 Sep 2022

HAL is a multi-disciplinary open access archive for the deposit and dissemination of scientific research documents, whether they are published or not. The documents may come from teaching and research institutions in France or abroad, or from public or private research centers.

L'archive ouverte pluridisciplinaire **HAL**, est destinée au dépôt et à la diffusion de documents scientifiques de niveau recherche, publiés ou non, émanant des établissements d'enseignement et de recherche français ou étrangers, des laboratoires publics ou privés.

Distributed under a Creative Commons Attribution - NonCommercial - NoDerivatives 4.0 International License

Check for updates

Received: 9 April 2022 | Revised: 24 July 2022 | Accepted: 26 July 2022

DOI: 10.1002/pat.5829

RESEARCH ARTICLE

polymers for advanced technologies WILEY

Highly crystalline hexagonal PbI_2 sheets on polyaniline/antimony tin oxide surface as a novel and highly efficient photodetector in UV, Vis, and near IR regions

Nomery M. A. Hadia[1,2] | Mohamed Shaban[3,4] | S. H. Mohamed[5] | Ali F. Al-Ghamdi[6] | Meshal Alzaid[1] | Asmaa M. Elsayed[3] | Abdel Hamid I. Mourad[7] | Mohammed A. Amin[8] | Rabah Boukherroub[9] | Ahmed Adel A. Abdelazeez[10] | Mohamed Rabia[3,11]

[1]Physics Department, College of Science, Jouf University, Sakaka, Saudi Arabia

[2]Basic Sciences Research Unit, Jouf University, Sakaka, Saudi Arabia

[3]Nanophotonics and Applications Lab, Physics Department, Faculty of Science, Beni-Suef University, Beni-Suef, Egypt

[4]Physics Department, Faculty of Science, Islamic University of Madinah, Madinah, Saudi Arabia

[5]Physics Department, Faculty of Science, Sohag University, Sohag, Egypt

[6]Chemistry Department, Faculty of Science, Taibah University, Al-Madinah, Saudi Arabia

[7]Mechanical Design Department, Faculty of Engineering, Helwan University, Cairo, Egypt

[8]Materials and Corrosion Group, Department of Chemistry, Faculty of Science, Taif University, Hawiya, Saudi Arabia

[9]University of Lille, CNRS, Centrale Lille, Université Polytechnique Hauts-de-France, UMR 8520 – IEMN, Lille, France

[10]Nanoscale Science, Chemistry Department, University of North Carolina at Charlotte, Charlotte, North Carolina, USA

[11]Nanomaterials Science Research Laboratory, Chemistry Department, Faculty of Science, Beni-Suef University, Beni-Suef, Egypt

Correspondence
Ahmed Adel A. Abdelazeez, Nanoscale Science, Chemistry Department, University of North Carolina at Charlotte, Charlotte, NC 28223, USA.
Email: aabdelh2@uncc.edu

Abstract

The work reports on the preparation of polyaniline/lead iodide optoelectronic photodetector on antimony tin oxide (ATO) glass (PANI/PbI_2/ATO) for providing a low-cost light sensor in the UV, Vis, and near IR regions (wide optical range photodetector). The deposition of PbI_2 nanoparticles was carried out on the surface of PANI using the ionic adsorption deposition method. Four ATO/PANI/PbI_2 composites (I, II, III, and IV) were produced by varying the Pb^{2+} concentrations (0.01, 0.03, 0.05, and 0.07 M, respectively). The chemical structure, morphology, optical, and electrical properties were assessed using different analytical tools. Scanning electron microscopy (SEM) imaging revealed the formation of a nanoporous PANI network. After PbI_2 incorporation within the PANI network, white nanoparticles formed on the surface. The average size of the PbI_2 nanoparticles was 220, 270, 280, and 320 nm for Pb^{2+} concentration of 0.01, 0.03, 0.05, and 0.07 M, respectively. Moreover, x-ray diffraction analysis confirmed PANI/PbI_2 composite formation, as witnessed by the appearance of new peaks at 12.77°, 34.31°, and 38.8 ° characteristic of PbI_2. Through the optical analyses, the band gap values of the PANI/PbI_2 composites I, II, III, and IV were 2.63, 2.51, 2.46, and 2.48 eV, respectively. ATO/composite III was applied as an optoelectronic device for detection the light under different intensities or wavelengths, in which the current density (J_{ph}) increase from 2.5 to 3.42 mA cm^{-2} upon increasing of the light intensity from 25 to 100 mW.cm^{-2}, respectively. Moreover, the J_{ph} recorded an optimum value of 3.33 mA cm^{-2} at 390 nm, which decreased to 2.09 mA cm^{-2} at 490 nm and increased again to 3.13 mA cm^{-2} at 636 nm. The optoelectronic photodetector exhibited an optimum incident photon to electron conversion efficiency (IPCE) of 10.7% at 390 nm. The photoresponsivity (R) and detectivity (D) were determined to be 107 mA cm^{-2} and 3.38 $\times 10^{10}$ Jones,

This is an open access article under the terms of the Creative Commons Attribution-NonCommercial-NoDerivs License, which permits use and distribution in any medium, provided the original work is properly cited, the use is non-commercial and no modifications or adaptations are made.
© 2022 The Authors. *Polymers for Advanced Technologies* published by John Wiley & Sons Ltd.

Mohamed Rabia, Nanophotonics and Applications Lab, Physics Department, Faculty of Science, Beni-Suef University, Beni-Suef 62514, Egypt.
Email: mohamedchem@science.bsu.edu.eg

Funding information
Deanship of Scientific Research at Jouf University, Grant/Award Number: DSR-2021-03-0321

respectively. Finally, a simple mechanism was proposed to account for the response of the prepared optoelectronic devices to the photon flux. Soon, our team will work on design an optoelectronic device that can be applied in the industrial field through the high technology device such as cameras and aircrafts for light detection.

KEYWORDS
ATO/PANI/PbI_2 composites, optical properties, photocatalytic activities

1 | INTRODUCTION

Optoelectronic photodetectors are very promising devices, owing to their applications in different fields such as streets lighting, smart windows, spacecraft, and cameras.[1–3] These optoelectronic devices facilitate light detection under different intensities and wavelengths. The light detection takes place through the activation of the photodetector materials with a photon flux that causes electronic level splitting, followed by hot electrons collection over the photodetector surface. These electrons produce J_{ph} and represent the rate of the photoelectrochemical process.

Many materials such as metal oxides, sulfides, and nitrides have been studied for light detection in various light regions.[1,4,5] The performance of photodetectors could be enhanced by increasing the density of active sites on their surface. One efficient route to achieve this goal is through the utilization of materials featuring high surface area. Therefore, nanomaterials such as nanorods, nanotubes, nanowires, and nanosheets have been widely investigated for light detection.[6–8]

Wang et al[9] fabricated a photodetector based on CuO nanowires for IR detection. The device exhibited low efficiency with a J_{ph} value of 20 μA at a bias voltage of +5 V. Bai et al[10] prepared ZnO/CuO nanocomposite photodetector and recorded a small J_{ph} value of 107 μA at +1 V. Hang et al[11] studied the ability of Si heterojunction as a photodetector, the device achieved a J_{ph} value of 4.5 μA at a bias voltage of 0 V. Moreover, PbI_2 doped Ag 5% nanostructure film was prepared by pulsed laser deposition and was applied as photodetector, the J_{ph} value was 0.2 mA at a bias voltage of 6 V.[12] The PbI_2/graphene composite nanoplates was applied as photodetector, the J_{ph} value was 0.4 μA at a bias voltage of 2 V.[13]

Conductive polymers represent a promising category of polymers applied in the energy field. The response of these polymers to the light flux depends on the electron–hole separation. For example, poly-3-hexylthiophene was applied as a photodetector layer inside the eye.[14] Other studies were carried out using iron-doped polymethylmethacrylate (Fe-doped PMMA)[15] and PMMA/styrene/carbon nanotubes composite[14] as optoelectronic materials for the light detection.[16] Polyvinylpyrrolidone/$CsPbBr_3$ composite was prepared and used as an optoelectronic device, the J_{ph} was 0.01 mA at 2 V.[17] Moreover, various studies were carried out on aniline derivatives such as triphenylamine as optoelectronic device, reaching a J_{ph} of 0.001 mA at 0 V.[18] The effect of fluorine-doped benzodithiophene was theoretically studied, revealing an enhancement in the optical properties of the polymer for the optoelectronic applications.[19] Moreover, Jha et al[20] has worked on recycling of nanofiber PANI-Pb nanocrystals waste for generating high-performance super-capacitor electrodes. Moreover, they were worked on nanofibers to nanocuboids of polyaniline self-assembled materials through which toxic heavy metal ions are automatically removed from aqueous solution.[21]

Although the previous literature revealed the benefits of the application of polymers as optoelectronic materials, there were many drawbacks related to the high-cost techniques for the preparation process, low optoelectronic efficiency, small *R* or *D* values, and low device reproducibility. Moreover, most of the previous literature focused on light detection in just a single region, UV, Vis, or near IR.

In our previous work, we synthesized TiO_2/TiN nanotubes using Al_2O_3 template; these tubes operated as a high efficient photodetector with IPCE, *R*, and *D* of 9.64%, 450 mA W^{-1}, and 8.0×10^{12} Jones, respectively.[22] Moreover, we have studied the effect of Au on the TiO_2/TiN nanotubes' performance. The device achieved an efficiency of 10.25%, with *R* and *D* values of 438 mA W^{-1} and 8.86×10^{12} Jones, respectively.[23] In addition to that, the effect of alkali metal on CdS performance was studied. IPCE, *D*, and *R* values of >10%, 1.5×10^{10} Jones, and 38 mA W^{-1} were recorded, respectively.[24]

Our current study alleviates the previous limitations through the synthesis of a high efficiency optoelectronic photodetector ATO/PANI/PbI_2, in which the geometric hexagonal PbI_2 is decorated inside PANI. This highly optical responding composite can detect the light in abroad light regions: UV, Vis, and IR. Moreover, the photodetector response to the light under different intensities from 25 to 100 mW cm^{-2} with high IPCE, *R*, and *D* values that represent the high light sensing efficiency. In addition to that, the device displayed high reproducibility for light sensing. Through our study, the utilization of an in situ polymerization process to deposit a porous polyaniline (PANI) layer on antimony tin oxide (ATO) glass was carried out. The PANI matrix assisted further deposition of PbI_2 nanosheets. The chemical structure, morphology, optical and electrical properties of the obtained materials were examined using different analytical tools. The influence of light intensity (25–100 mW cm^{-2}) and wavelength (390–636 nm) on the device performance was studied. Finally, a plausible mechanism was proposed for the light sensing using the polymer composite optoelectronic device.

2 | EXPERIMENTAL SECTION

2.1 | Materials

$Pb(NO_3)_2$ was purchased from El Naser chemical Co., Egypt. Aniline, iodine (I_2), and potassium iodide (KI) were bought from Biochem Company, Egypt. Silver paste, acetic acid (CH_3COOH), and ammonium persulfate ($[NH_4]_2S_2O_8$) were obtained from Alpha chemical Co., Egypt. ATO glass was purchased from American Elements, USA.

2.2 | Preparation of PANI/PbI_2 on antimony tin oxide glass

Polyaniline (PANI) was prepared through an in situ oxidation polymerization method on ATO glass. A volume of 50 ml of aniline (0.1 M) was dissolved in 0.5 M CH_3COOH under ultrasonication (at room temperature for 30 min). Separately, 50 ml of 0.15 M $(NH_4)_2S_2O_8$ (oxidant) was nicely dispersed in 0.5 M CH_3COOH under ultrasonication. Then, the oxidant solution was added dropwise onto the aniline solution in the presence of an ATO glass. After 1 h, PANI precipitate was formed over the ATO glass. The ATO/PANI was dried at 60°C for 6 h and then dipped in $Pb(NO_3)_2$ solution (50 ml) at different concentrations (0.01–0.1 M) for 2 h at 298 K. The resulting ATO/PANI/Pb^{2+} film was dipped into 0.01 M I_2 aqueous solution (50 ml) for 15 min. During this process, PbI_2 precipitates and coats of the PANI network. This reaction carried out at room temperature, this led to the arrangement of PbI_2 on the PANI surface during the composite formation. The optimum ATO/PANI/PbI_2 composite was determined from the optimum light absorbance values through optical absorption analyses. By varying the Pb^{2+} concentration (0.01, 0.03, 0.05, and 0.07 M), ATO/PANI/PbI_2 composites I, II, III, and IV are prepared, respectively. The hexagonal PbI_2 shape on the PANI surface increases the light absorption properties.

2.3 | Characterization

X-ray diffraction (XRD) patterns of the samples were recorded on a Bruker D8 advance diffractometer using Cu Kα radiation ($\lambda = 0.15418$ nm). The morphology of the samples was studied by a field-emission scanning electron microscope (FE-SEM, Hitachi, S-4800) at an acceleration voltage of 5.0 kV. The optical analyses of the samples were carried out using a double beam spectrophotometer (Perkin Elmer Lamba 950, USA). Raman spectra were performed using Enwave Raman microscopy (spot 1 μm) with a 532 nm laser excitation.

2.4 | Electrochemical measurements

All the electrochemical measurements were carried out using the electrochemical workstation (CHI660E) through the voltage range from −1 to +1 V, as shown in Figure 1. The electrochemical measurements were acquired under a Xenon lamp, in which ATO and ATO/PANI/PbI_2/Ag represent the two sides electrodes of the photodetector. The effect of light intensity (25–100 mW cm^{-2}) and light wavelength (390–636 nm) on the prepared photodetector performance was assessed. Moreover, the reproducibility and dark current were evaluated. The measurements were carried out at 25°C in air environment.

3 | RESULTS AND DISCUSSION

3.1 | Structural, optical, and morphological properties

The XRD plots of the prepared PANI and PANI/PbI_2 composites (I, II, III, and IV) are shown in Figure 2A. The PANI peaks (black line) appeared at $2\theta = 20.78°$ and 25.55° and are assigned respectively to the (021) and (200) diffraction planes. These semi-sharp peaks indicate the lamellar structure nature of the prepared PANI.[25]

After PANI/PbI_2 formation, there is an obvious shift in the PANI peak located at 25.55°–26.05°, and the peak intensity increases from composite I to III. The shifts in the peak is related to the composite formation, the increasing in the intensity indicate high crystallinity of the formed composite.[26,27]

Moreover, after composite formation, there is an appearance of new peaks at 12.77°, 34.31°, and 38.8 ° characteristic of PbI_2.[28] The crystal size of composite III was determined to be 33.3 nm (for the peak at 12.77°) using the Scherrer equation (Equation 1):

$$D = 0.94\lambda/ß\cos\theta \quad (1)$$

ß denotes the full-width half maximum,[29] λ is the wavelength (0.154 nm), and θ corresponds to the Bragg's angle.

The Raman spectra of PANI and its PbI_2 composites I, II, III, and IV are depicted in Figure 2B. From these results, one clearly sees some differences in the peaks related to the PANI and PANI/PbI_2 composites, proving PbI_2 incorporation in the PANI network. The Raman peaks at 1584 and 1489 cm^{-1} are related to the C—C and N—H benzene ring vibrations, respectively.[30] The peaks at 1160 and 1220 cm^{-1} are related to the C—H stretching vibrations.[31,32] These peaks increase with increasing of the PbI_2 concentration from composite I to III, then decrease in composite IV. Moreover, the peak at 400 cm^{-1} in the PANI (black line) is related to the in-plane vibration modes. The peak at 180 cm^{-1} is characteristic of the $A_1{}^2$ hexagonal vibration mode of PbI_2,[33] Moreover, this peak confirms the crystallinity of the PbI_2 material.[34] The effect of crystallinity of PbI_2 appears clearly in the composite III that has the optimum intensities of the peaks in comparison with other composites. The results are in full accordance with the XRD analyses.

The optical absorption spectra of the PANI and PANI/PbI_2 composites are displayed in Figure 2C. The PANI absorption peaks are located in the UV region at 325 nm and in the Vis region at 450 and 600 nm. After the formation of the PANI/PbI_2 composites, the peak intensities at 325 and 600 nm increased, and new additional peak at

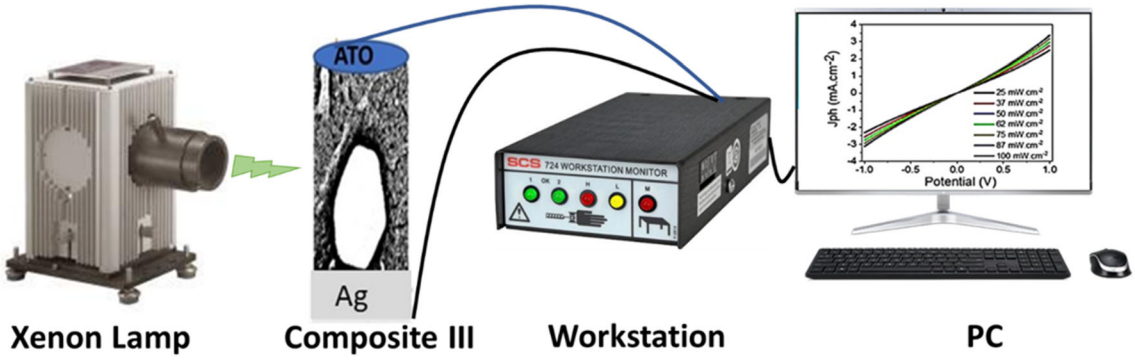

FIGURE 1 The schematic diagram of the ATO/PANI/PbI_2 photodetector electrochemical measurements using the power station under xenon lamp irradiation. ATO, antimony tin oxide; PANI, polyaniline

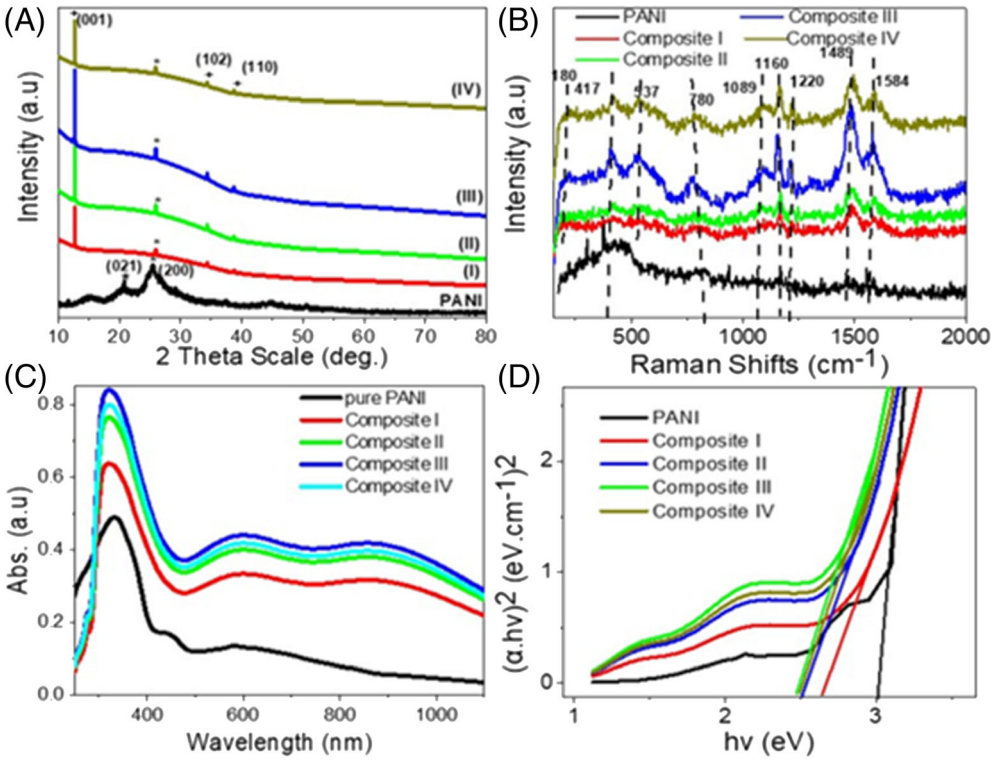

FIGURE 2 (A) XRD patterns, (B) Raman spectra, (C) optical absorbance, and (D) optical bandgap of PANI and PANI/PbI_2 composites I, II, III, and IV. PANI, polyaniline; XRD, x-ray diffraction

878 nm appeared in the IR region. The increasing in the peak intensity indicates the enhancement in the optical properties related to high light response.[35] The peaks in the UV or Vis regions are related to the band-to-band electron transitions, while the peak in the IR region is related to the electron vibrations. The intensities of the peaks reached their optimum values in the composite III, in agreement with the XRD and Raman analyses.

The optical bandgap can be determined using the Kubelka–Munk equations (Equations 2–4)[36] using molar absorption coefficient (*K*) and scattering factor (*S*), as shown in Figure 2D. A bandgap of 3.0 eV was determined for PANI, this value well-matched with the recently-reported values.[25,37] The band gap values of the PANI/PbI_2 composites I, II, III, and IV were 2.63, 2.51, 2.46, and 2.49 eV, respectively. The enhancements in the bandgap values are related to the composite formation (PANI and PbI_2) which accept a highly optical properties for enhancement its applications as a light detection device, in which the composite III has the optimum bandgap (2.46 eV). This value favors the application of the composite III as an optoelectronic device, owing to its ability of light sensing through electron motion behavior.

$$F(R) = \frac{K}{S} \tag{2}$$

$$K = (1 - R)^2 \tag{3}$$

$$S = 2R \tag{4}$$

The morphologies of the prepared PANI and PANI/PbI_2 composites are assessed using SEM imaging (Figure 3). The SEM image of PANI in Figure 3A exhibits a homogeneous and porous polymer layer. The surface has a particle size of about 40 nm. In the SEM images of PANI/PbI_2 composites, PbI_2 white spots covering the PANI network are

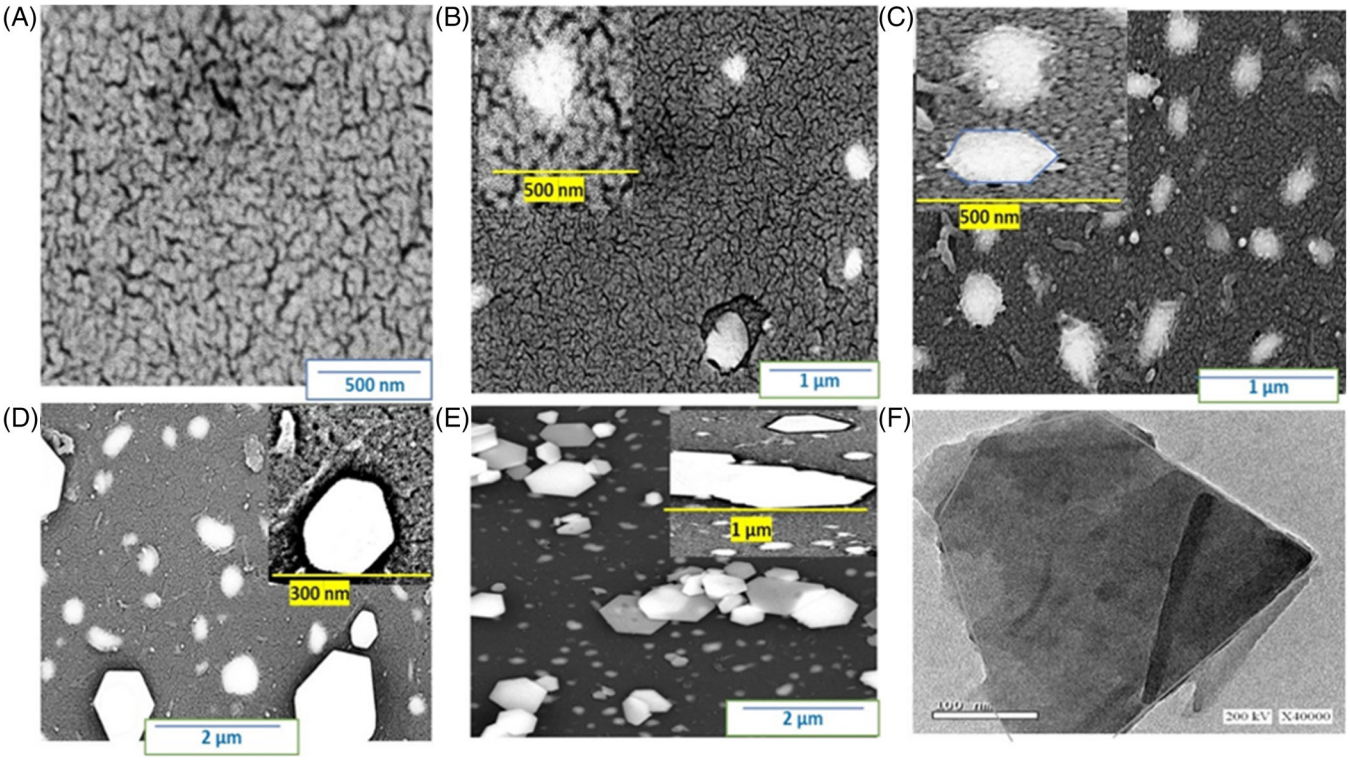

FIGURE 3 SEM images of (A) PANI, (B) composite I, (C) composite II, (D) composite III, and (E) composite IV. (F) TEM image of composite III. PANI, polyaniline; SEM, scanning electron microscopy

visible. These PbI_2 white spots increase in number and size from composite I to III, Figure 3B–E, respectively. In addition to that, the PbI_2 particles exhibit hexagonal shapes and form sheets over the surface of composites III and IV. The PbI_2 average particle size increased with increasing of the Pb^{2+} concentration to reach 220, 270, 280 and 320 nm for composites I, II, III and IV, respectively.

TEM image of the composite III (Figure 3F) confirms that the PbI_2 crystalline sheets grew throughout the PANI network with a particle size of about 280 nm.

The surface morphologies and cross-sections are confirmed with the software program (ImageJ), as shown in Figure 4. This software confirms the roughness behavior obtained from SEM analyses. From Figure 4A, PANI owns a rough uniform nonporous structure. The film thickness is about 580 nm. After composites' formation, the PbI_2 particles appear like obelisks that penetrate the PANI network with cuboid and hexagonal structure. These obelisks shape increases in height and thickness from composite I to IV. The overall film thickness for the composites was about 1000 nm. The PbI_2 has the optimum distribution in composite III, in accordance confirm with XRD, Raman, and optical analyses.

3.2 | The photodetector electrochemical study

3.2.1 | Effect of light intensity on the current density

The influence of light intensity on the produced current density (J_{ph}) of the optoelectronic photodetector, ATO/PANI/PbI_2 (composite III), was assessed and the results are presented in Figure 5A. Also, the recorded J_{ph} values at a bias of +1.0 V under light illumination are shown in Figure 5B. The results evidenced an increase in the J_{ph} values from 2.5 to 3.42 mA cm^{-2} upon increasing of the light intensity from 25 to 100 mW cm^{-2}, respectively. This increase is related to the high sensitivity of the ATO/PANI/PbI_2 photodetector to light illumination, which was able to detect small light intensity variation.[38] Under light illumination, the photodetector accepts more photons and liberates photoelectrons, which are collected on the surface, leading to enhanced current density, J_{ph}. Moreover, J_{ph} values represent the light response due to the total electrons collected on the surface after their transfer from the valence band to the conduction band; the generated holes are collected on the other electrode side.[29,39,40] The nonlinear relation indicates the generation of a Schottky barrier with the complex relation of holes and electrons.[41]

The high J_{ph} values of 3.42 mA cm^{-2}, recorded in a small potential range (−1 to +1 V), originates from the high surface area of the ATO/PANI/PbI_2, owing to its high roughness and porous nature. These features increase the light sensing, especially with incorporating the PbI_2 light spots that can detect even a small number of photons.

The reproducibility study of the ATO/PANI/PbI_2 is displayed in Figure 5C under three separate runs. It is clear that the photodetector has great reproducibility with a standard deviation of 1.1%, reflecting the stability of the photodetector for light detection and sensing.

The dark current (J_d), due to charge accumulation under applied voltage, is presented in Figure 5D. The values recorded from −1 to +1 V are small in comparison with the J_{ph} values acquired under light irradiation.[22]

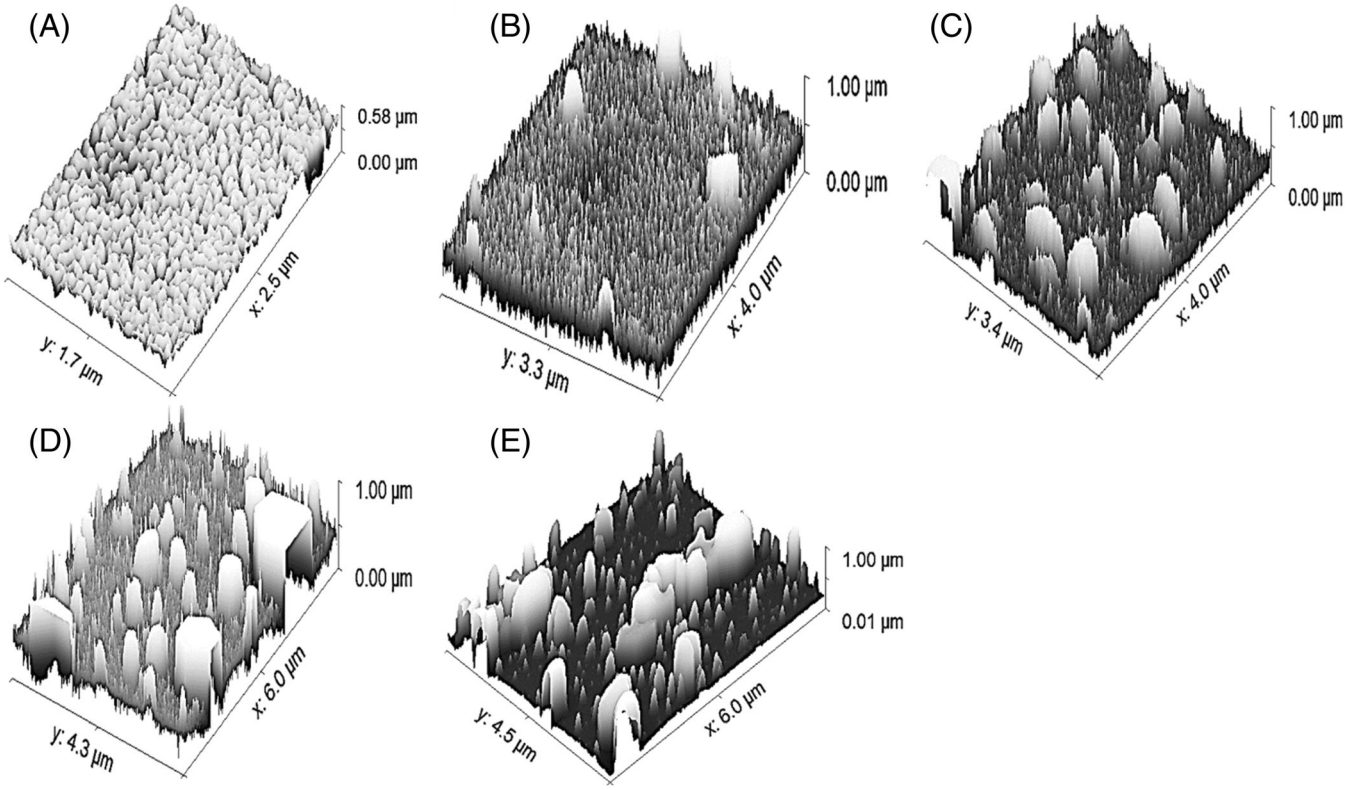

FIGURE 4 The surface roughness and cross-section of (A) polyaniline, (B) composite I, (C) composite II, (D) composite III, and (E) composite IV

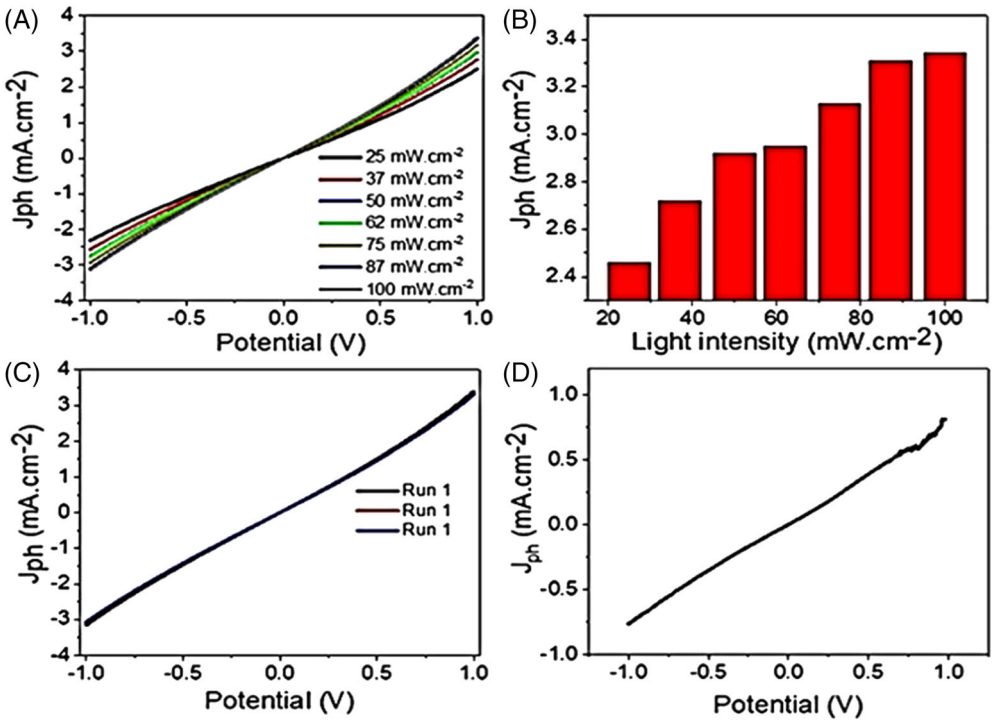

FIGURE 5 (A) The influence of light intensity, (B) current density recorded at +1.0 V versus light intensity, (C) reproducibility, and (D) dark current of the ATO/PANI/PbI_2 photodetector at 25°C. ATO, antimony tin oxide; PANI, polyaniline

3.2.2 | Influence of light wavelength on the current density

The effect of the monochromatic light (390–636 nm) on the ATO/PANI/PbI_2 photodetector is summarized in Figure 6A. The monochromatic light has a great influence on the photodetector response; the J_{ph} reached an optimum value of 3.33 mA cm^{-2} at 390 nm, which decreased continuously to 2.09 mA cm^{-2} at 490 nm. Then, there is an increase in the J_{ph} value again to 3.13 mA cm^{-2} at 636 nm. The variation in the J_{ph} values matched well with the optical

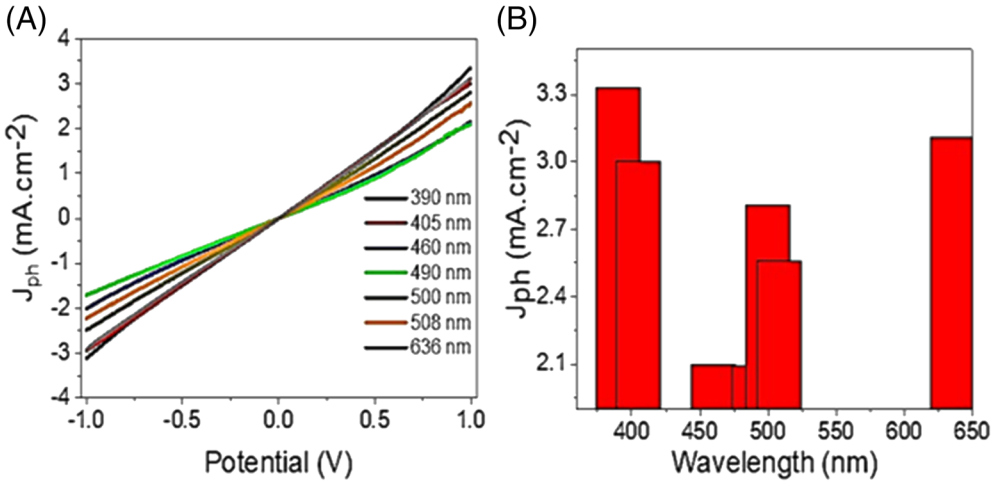

FIGURE 6 (A) The response of the ATO/PANI/PbI_2 photodetector and (B) the recorded J_{ph} values at +1.0 V under different monochromatic light wavelengths from 390 to 636 nm. ATO, antimony tin oxide; PANI, polyaniline

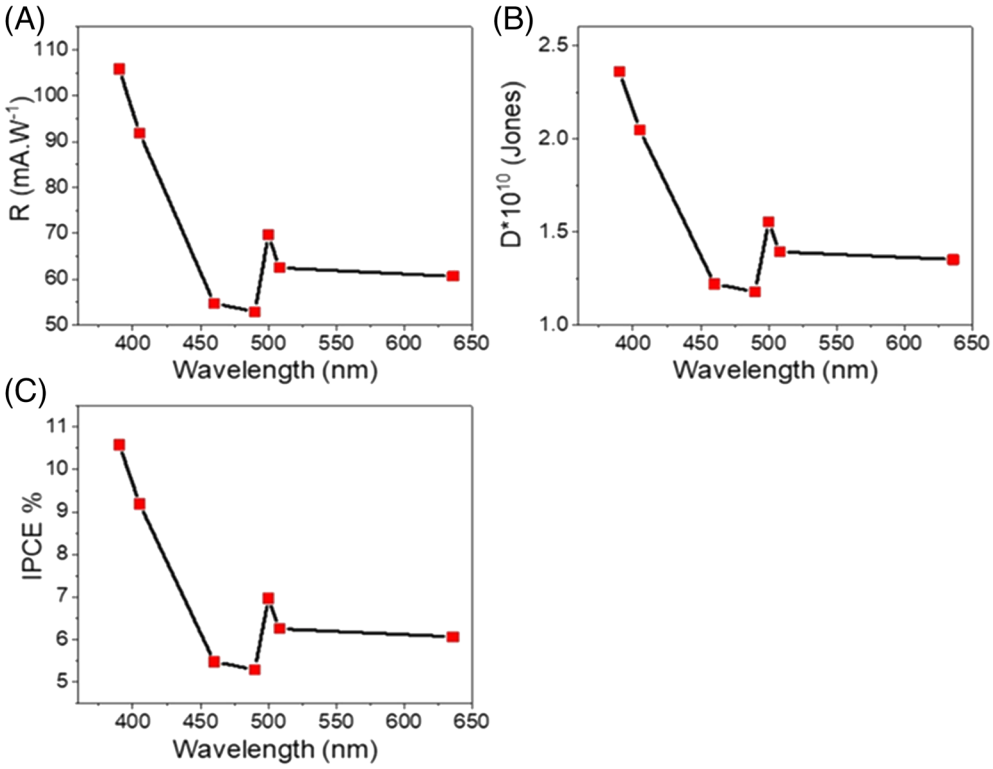

FIGURE 7 (A) *R*, (B) *D*, and (C) IPCE values of the ATO/PANI/PbI_2 photodetector. ATO, antimony tin oxide; PANI, polyaniline

absorption curve in Figure 2C. This behavior is clearly highlighted through the relation between the wavelengths and the recorded J_{ph} values at a constant potential of +1.0 V (Figure 6B). The J_{ph} values correspond to the light detection and sensing behavior.[39,42,43]

The high J_{ph} value on the blue side is related to the high light frequency, while the high value on the red side is ascribed to the electron vibrations for the unsaturation properties in the IR region.[42,44] These properties indicate the ability of the ATO/PANI/PbI_2 photodetector to respond to light over a broad optical region including UV, Vis, and IR. So, the prepared photodetector is a unique device for light responding in these regions, with the great advantages of the very low cost that qualifies this photodetector for potential industrial applications.

3.2.3 | The efficiency of the optoelectronic device

The efficiency of the ATO/PANI/PbI_2 photodetector depends on many parameters: IPCE, *R*, and *D* values. The *R* values depend on both J_{ph} and J_d under light irradiation and dark, respectively[45] along with the light intensity value (*P*), as shown in Equation (5).[46] This relation is represented in Figure 7B for different wavelengths. The results indicate that the prepared photodetector respond to light in a broad wavelength range from UV/Vis to near IR. The optimum photoresponsivity was 107 mA W^{-1} at 390 nm.

The *D* value of the photodetector mainly depends on the *R* values, surface area (*A*), electron charge (*e*) and dark current, as shown in Equation (6) and Figure 7B. The device achieved an optimum

TABLE 1 Comparison of the performance of the prepared ATO/PANI/PbI_2 photodetector with previous works

Structure [reference]	Wavelength (nm)	Bias (V)	R (mA W^{-1})
Polyaniline/MgZnO[49]	250	5	0.1
Diketopyrrolopyrrole[50]	390	0.1	36
Graphene/P3HT[51]	325	1	N/A
N,N′-dioctyl-3,4,9,10-perylenedicarboximide[52]	480	1	20
TiO_2-PANI[53]	320	0	3
2,1,3-benzothiadiazole[19]	734	0	N/A
PbI_2-5%Ag[12]	532	6	N/A
PbI_2-graphene[13]	550	2	N/A
GO/Cu_2O[54]	300	2	0.5
CuO nanowires[9]	390	5	-
ZnO/Cu_2O[10]	350	2	4
ZnO-CuO[55]	405	1	3
CuO/Si nanowires[11]	405	0.2	3.8
TiN/TiO_2[38]	550	5	-
Se/TiO_2[56]	450	1	5
TiO_2/NiO[57]	350	0	0.4
Graphene/GaN[58]	365	7	3
ZnO /RGO[59]	350	5	1.3
Al-CdS[60]	532	5	0.1
CdS-ZnO[61]	460	1	-
CdS[62]	840	-	3.8
ZnO/graphene/CdS[63]	365	0	2.7
TiN/TiO_2[38]	550	5	-
Se/TiO_2[56]	450	1	5
GO/Cu_2O[54]	300	2	0.5
ATO/PANI/PbI_2 (this work)	390	1	107

Abbreviations: ATO, antimony tin oxide; PANI, polyaniline.

D value of 3.38×10^{10} (Jones) at 390 nm and decreased to 1.16×10^{10} Jones at 490 nm, followed by a small increase to reach 1.36×10^{10} Jones at 636 nm. The large D values of the photodetector confirm its responsivity to different light wavelengths (UV, Vis, and near IR).

The IPCE[47] of the ATO/PANI/PbI_2 photodetector was calculated using Equation (7),[48] and the obtained results are depicted in Figure 7C. The IPCE, corresponding to the electrons collected following the photon flux, reached an optimum value of 10.7% at 390 nm. This value decreased at 490 nm and increased again at 636 nm to 5.17% and 6%, respectively. Although there are variables in the IPCE values, the photodetector still features high values in all light regions. This property is related to the light absorption over a broad wavelength range. All these properties are related to the construction of the optoelectronic photodetector, in which the PbI_2 has a great light absorption that can capture effectively the photons, and then transfer them to the PANI network to generate a photocurrent. So, the prepared ATO/PANI/PbI_2 photodetector operates well under different light intensities and wavelengths, which qualifies it for potential industrial applications.

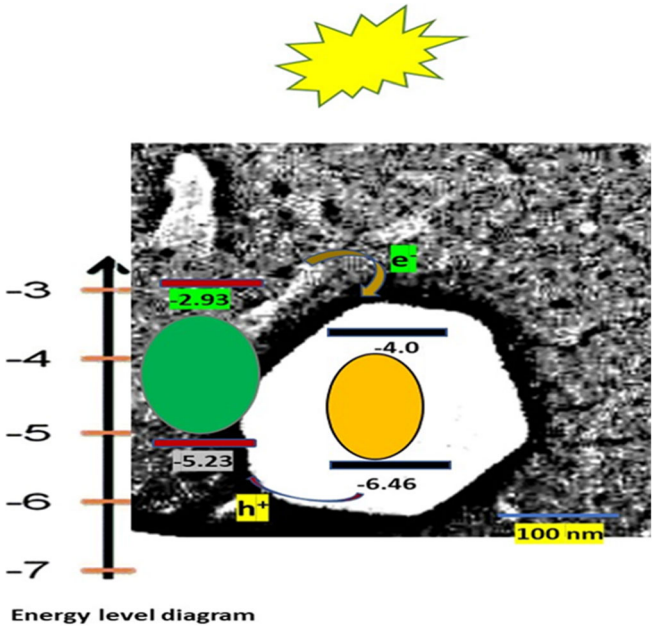

FIGURE 8 The mechanism of the ATO/PANI/PbI_2 optoelectronic photodetector device. ATO, antimony tin oxide; PANI, polyaniline

$$R = \frac{J_{ph} - J_d}{P} \quad (5)$$

$$D = R\sqrt{A/2eJ_d} \quad (6)$$

$$\mathrm{EQE} = R\frac{1240}{\lambda}100 \quad (7)$$

The recorded IPCE, *R*, and *D* values of the prepared ATO/PANI/PbI_2 optoelectronic photodetector are compared with the previous results, as shown in Table 1. From this comparison, the prepared ATO/PANI/PbI_2 optoelectronic device has a great photoresponsivity at a small bias voltage (1.0 V) in the visible region. This confirms the high sensitivity and detection of the light photons. These properties with the previous advantages qualify our photodetector for industrial applications.

3.3 | The mechanism of the light sensing

The plausible mechanism of light sensing by the ATO/PANI/PbI_2 optoelectronic device is explained using the energy band theory (Figure 8). The porous network nature of PANI and the PbI_2 nanomaterials with high light absorption behavior cause the creation of a bandgap. Upon light irradiation, electron–hole pairs are formed and the photoelectrons are collected at the surface.[64,65] The bandgap of the PANI/PbI_2 composite is 2.46 eV, with a small depletion layer due to the transfer of electrons from the PANI to the PbI_2 surface. This depletion layer appears as a Schottky barrier that forms the leakage in the behavior of the current–voltage curves. Although the presence of the Schottky barrier, there is a transfer of many hot electrons from the PANI surface to PbI_2, which is reflected by the high J_{ph} value of 3.42 mA cm^{-2} (Figure 5A). This behavior confirms that there is a continuous free electron flow with no carrier recombination.[66] After the electron transfer, the energy transfer due to the surface plasmonic resonance (localized SPR) appears through the electrons. These phenomena cause the accumulation of electrons on the PbI_2 surface, resulting in high J_{ph} values. The hexagonal sheets of PbI_2 (highly crystalline) increase the light capture through its small bandgap, and then increases the electron collections in its surface.[67]

4 | CONCLUSIONS

A novel optoelectronic photodetector, ATO/PANI/PbI_2 was prepared and assessed for light detection over a wide optical region ranging from UV, Vis, to near IR. The optoelectronic device responded to various light intensities from 25 to 100 mW.cm^{-2} to produce enhanced current densities, J_{ph}, values of 2.5–3.42 mA cm^{-2}, respectively. Moreover, the photodetector has an excellent response to various wavelengths (390–636 nm), with a J_{ph} value of 3.33 mA cm^{-2} recorded at 390 nm. This value decreased to 2.09 mA cm^{-2} at 490 nm and increased again to 3.13 mA cm^{-2} at 636 nm. Moreover, the photodetector achieved optimum IPCE, *R*, and *D* values of 10.7%, 107 mA W^{-1}, and 3.38 $\times$ 10^{10} Jones, respectively. The ATO/PANI/PbI_2 photodetector was qualified for its reproducibility, response to various light intensities, and operation under various light wavelengths (UV, Vis, and near IR). The obtained results combined with the low cost and easy preparation hold great promise for industrial application of the developed ATO/PANI/PbI_2 photodetector.

ACKNOWLEDGMENTS

The authors extend their appreciation to the Deanship of Scientific Research at Jouf University for funding this work through research grant no. DSR-2021-03-0321.

CONFLICT OF INTEREST

The authors declare no conflict of interest.

DATA AVAILABILITY STATEMENT

The data that support the findings of this study are available from the corresponding author upon reasonable request.

ORCID

Nomery M. A. Hadia https://orcid.org/0000-0001-6133-546X
Meshal Alzaid https://orcid.org/0000-0002-2585-0138
Abdel Hamid I. Mourad https://orcid.org/0000-0002-8356-0542
Ahmed Adel A. Abdelazeez https://orcid.org/0000-0003-4641-6223
Mohamed Rabia https://orcid.org/0000-0001-6263-0604

REFERENCES

1. Zhong F, Wang H, Wang Z, et al. Recent progress and challenges on two-dimensional material photodetectors from the perspective of advanced characterization technologies. *Nano Res*. 2021;14:1840-1862.
2. Liu C, Guo J, Yu L, et al. Silicon/2D-material photodetectors: from near-infrared to mid-infrared. *Light Sci Appl*. 2021;10:123.
3. Maiti R, Patil C, Saadi MASR, Strain-engineered high-responsivity MoTe2 photodetector for silicon photonic integrated circuits. *Nat Photonics*. 2020;149(14):578-584.
4. Flöry N, Ma P, Salamin Y, et al. Waveguide-integrated van der Waals heterostructure photodetector at telecom wavelengths with high speed and high responsivity. *Nat Nanotechnol*. 2020;152(15):118-124.
5. Fan P, Chettiar UK, Cao L, Afshinmanesh F, Engheta N, Brongersma ML. An invisible metal–semiconductor photodetector. *Nat. Photonics*. 2012;66(6):380-385.
6. Rabia M, Mohamed SH, Zhao H, Shaban M, Lei Y, Ahmed AM. Correction to: TiO2/TiOxNY hollow mushrooms-like nanocomposite photoanode for hydrogen electrogeneration. *J Porous Mater*. 2019;271(27):329.
7. Almohammedi A, Shaban M, Mostafa H, Rabia M. Nanoporous TiN/TiO2/alumina membrane for photoelectrochemical hydrogen production from sewage water. *Nanomater*. 2021;11:2617.
8. Elsayed AM, Shaban M, Aly AH, Ahmed AM, Rabia M. Preparation and characterization of a high-efficiency photoelectric detector composed of hexagonal Al_2O_3/TiO_2/TiN/Au nanoporous array. *Mater Sci Semicond Process*. 2022;139:106348.
9. Wang SB, Hsiao CH, Chang SJ, et al. A CuO nanowire infrared photodetector. *Sensors Actuators A Phys*. 2011;171:207-211.

10. Bai Z, Zhang Y. Self-powered UV–visible photodetectors based on ZnO/Cu_2O nanowire/electrolyte heterojunctions. *J Alloys Compd*. 2016;675:325-330.
11. Hong Q, Cao Y, Xu J, Lu H, He J, Sun JL. Self-powered ultrafast broadband photodetector based on p-n heterojunctions of CuO/Si nanowire array. *ACS Appl Mater Interfaces*. 2014;6:20887-20894.
12. Ismail RA, Mousa AM, Shaker SS. Visible-enhanced silver-doped PbI2 nanostructure/Si heterojunction photodetector: effect of doping concentration on photodetector parameters. *Opt Quantum Electron*. 2019;51:1-19.
13. Chen Z, Ci H, Tan Z, et al. Growth of 12-inch uniform monolayer graphene film on molten glass and its application in PbI 2-based photodetector. 1888-1893. doi:10.1007/s12274-019-2453-1
14. Yuan B, Aziz MRF, Li S, Wu J, Li D, Li RK. An electro-spun tricomponent polymer biomaterial with optoelectronic properties for neuronal differentiation. *Acta Biomater*. 2021;139:82-90. doi:10.1016/J.ACTBIO.2021.05.036
15. AlAbdulaal TH, Yahia IS. Analysis of optical linearity and nonlinearity of Fe3+− doped PMMA/FTO polymeric films: new trend for optoelectronic polymeric devices. *Phys B Condens Matter*. 2021;601:412628.
16. Shankar U, Gupta CR, Oberoi D, Singh BP, Kumar A, Bandyopadhyay A. A facile way to synthesize an intrinsically ultraviolet-C resistant tough semiconducting polymeric glass for organic optoelectronic device application. *Carbon N Y*. 2020;168:485-498.
17. Fulari AV, Duong NT, Nguyen DA, et al. Achieving direct electrophoretically deposited highly stable polymer induced CsPbBr3 colloidal nanocrystal films for high-performance optoelectronics. *Chem Eng J*. 2021;433:133809. doi:10.1016/J.CEJ.2021.133809
18. Yen HJ, Liou GS. Design and preparation of triphenylamine-based polymeric materials towards emergent optoelectronic applications. *Prog Polym Sci*. 2019;89:250-287.
19. Liu Y, Guo P, Gao P, et al. Effect of fluorine atoms on optoelectronic, aggregation and dielectric constants of 2,1,3-benzothiadiazole-based alternating conjugated polymers. *Dye Pigment*. 2021;193:109486.
20. Jha PK, Singh SK, Gatla S, Mathon O, Kurungot S, Ballav N. Pb2+-N bonding chemistry: recycling of polyaniline-Pb nanocrystals waste for generating high-performance supercapacitor electrodes. *J Phys Chem C*. 2016;120:911-918.
21. Jha PK, Dhara B, Ballav N. Nanofibers to nanocuboids of polyaniline by lead nitrate: hierarchical self-assembly with lead ions. *RSC Adv*. 2014;4:9851-9855.
22. Elsayed AM, Rabia M, Shaban M, Aly AH, Ahmed AM. Preparation of hexagonal nanoporous Al_2O_3/TiO_2/TiN as a novel photodetector with high efficiency. *Sci. Rep*. 2021;111(11):1-12.
23. Li C, Wang F, Xu J, et al. Efficient perovskite/fullerene planar heterojunction solar cells with enhanced charge extraction and suppressed charge recombination. *Nanoscale*. 2015;7:9771-9778.
24. Baran Aydin E. Fabrication and characterization of CuO nanostructures: applications in Electrocatalytic hydrogen production. *Çukurova Univ J Fac Eng Archit*. 2020;35:127-138.
25. Abukhadra MR, Rabia M, Shaban M, Verpoort F. Heulandite/polyaniline hybrid composite for efficient removal of acidic dye from water; kinetic, equilibrium studies and statistical optimization. *Adv Powder Technol*. 2018;29:2501-2511.
26. Liu J, Shen J, Wang J, et al. Polymeric ionic liquid—assisted polymerization for soluble polyaniline nanofibers. *Front Chem Sci Eng*. 2021;15:118-126.
27. Qiu T, Yang JG, Bai XJ, Wang YL. The preparation of synthetic graphite materials with hierarchical pores from lignite by one-step impregnation and their characterization as dye absorbents. *RSC Adv*. 2019;9:12737-12746.
28. Zhang H, Tao M, Gao B, et al. Preparation of CH3NH3PbI3 thin films with tens of micrometer scale at high temperature. *Sci. Rep*. 2017;71(7):1-9.
29. Shaban M, Rabia M, Eldakrory MG, Maree RM, Ahmed AM. Efficient photoselectrochemical hydrogen production utilizing of $APbI_3$ (A=Na, Cs, and Li) perovskites nanorods. *Int. J. Energy Res*. 2020;45:6326. doi:10.1002/er.6326
30. Sci-Hub | Electropolymerization of polyaniline thin films. *High Perform Polym*. 2014;26(6):641-646. doi:10.1177/0954008314538081
31. Shakoor A, Rizvi TZ, Nawaz A. Raman spectroscopy and AC conductivity of polyaniline montmorillonite (PANI-MMT) nanocomposites. *J Mater Sci Mater Electron*. 2011;22:1076-1080.
32. Rajagopalan B, Hur SH, Chung JS. Surfactant-treated graphene covered polyaniline nanowires for supercapacitor electrode. *Nanoscale Res Lett*. 2015;10:1-9.
33. Frisenda R, Island JO, Lado JL, et al. Characterization of highly crystalline lead iodide nanosheets prepared by room-temperature solution processing. *Nanotechnology*. 2017;28:455703.
34. Wangyang P, Sun H, Zhu X, Yang D, Gao X. Mechanical exfoliation and Raman spectra of ultrathin PbI2 single crystal. *Mater Lett*. 2016;168:68-71.
35. Wang H, Wen H, Hu B, et al. Facile approach to fabricate waterborne polyaniline nanocomposites with environmental benignity and high physical properties. *Sci Rep*. 2017;71(7):1-12.
36. Mohamed HSH, Rabia M, Zhou XG, et al. Phase-junction ag/TiO2 nanocomposite as photocathode for H2 generation. *J Mater Sci Technol*. 2021;83:179-187.
37. Shaban M, Abukhadra MR, Rabia M, Elkader YA, Abd El-Halim MR. Investigation the adsorption properties of graphene oxide and polyaniline nano/micro structures for efficient removal of toxic Cr(VI) contaminants from aqueous solutions; kinetic and equilibrium studies. *Rend Lincei*. 2018;29:141-154.
38. Naldoni A, Guler U, Wang Z, et al. Broadband hot-electron collection for solar water splitting with Plasmonic titanium nitride. *Adv Opt Mater*. 2017;5:1601031-1601042.
39. Rabia M, Shaban M, Adel A, Abdel-Khaliek AA. Effect of plasmonic au nanoparticles on the photoactivity of polyaniline/indium tin oxide electrodes for water splitting. *Environ Prog Sustain Energy*. 2019;38:13171.
40. Helmy A, Rabia M, Shaban M, Ashraf AM, Ahmed S, Ahmed AM. Graphite/rolled graphene oxide/carbon nanotube photoelectrode for water splitting of exhaust car solution. *Int J Energy Res*. 2020;44:7687-7697.
41. Wang X, Tian W, Liao M, Bando Y, Golberg D. Recent advances in solution-processed inorganic nanofilm photodetectors. *Chem Soc Rev*. 2014;43:1400-1422.
42. Mohamed F, Rabia M, Shaban M. Synthesis and characterization of biogenic iron oxides of different nanomorphologies from pomegranate peels for efficient solar hydrogen production. *J Mater Res Technol*. 2020;9:4255-4271.
43. Rabia M, Shaban M, Jibali BM, Abdelkhaliek AA. Effect of annealing temperature on the photoactivity of ITO/VO_2 (M)/Au film electrodes for water splitting. *J Nanosci Nanotechnol*. 2020;20:4120-4130.
44. Liu Z, Li F, Li S, et al. Fabrication of UV photodetector on TiO_2 diamond film. *Sci Rep*. 2015;5:14420.
45. Jia R, Zhao D, Gao N, Liu D. Polarization enhanced charge transfer: dual-band GaN-based plasmonic photodetector. *Sci Rep*. 2017;7:1-8.
46. Kunwar S, Pandit S, Jeong JH, Lee J. Improved photoresponse of UV photodetectors by the incorporation of plasmonic nanoparticles on GaN through the resonant coupling of localized surface plasmon resonance. *Nano-Micro Lett*. 2020;12:1-16.
47. Zhao H, Ouyang B, Han L, Mishra YK, Zhang Z, Yang Y. Conjuncted photo-thermoelectric effect in ZnO–graphene nanocomposite foam for self-powered simultaneous temperature and light sensing. *Sci Rep*. 2020;10:11864.
48. Shaban M, Rabia M, El-Sayed AMA, Ahmed A, Sayed S. Photocatalytic properties of PbS/graphene oxide/polyaniline electrode for hydrogen generation. *Sci Rep*. 2017;7:1-13.

49. Chen H, Yu P, Zhang Z, et al. Ultrasensitive self-powered solar-blind deep-ultraviolet photodetector based on all-solid-state polyaniline/MgZnO bilayer. *Small*. 2016;12:5809-5816.
50. Hu L, Qiao W, Qi J, Zhang X, Han J, Wang C. Significant enhancement of photodetector performance by subtle changes in the side chains of dithienopyrrole-based polymers. *RSC Adv*. 2016;6:22494-22499.
51. Tan WC, Shih WH, Chen YF. A highly sensitive graphene-organic hybrid photodetector with a piezoelectric substrate. *Adv Funct Mater*. 2014;24:6818-6825.
52. Kim JS, Choi YJ, Woo HJ, et al. Schottky-barrier-controllable graphene electrode to boost rectification in organic vertical P-N junction photodiodes. *Adv Funct Mater*. 2017;27:1704475.
53. Zheng L, Yu P, Hu K, Teng F, Chen H, Fang X. Scalable-production, self-powered TiO_2 Nanowell-organic hybrid UV photodetectors with tunable performances. *ACS Appl Mater Interfaces*. 2016;8:33924-33932.
54. Lan T, Fallatah A, Suiter E, Padalkar S. Size controlled copper (I) oxide nanoparticles influence sensitivity of glucose biosensor. *Sensors*. 2017;17:1944.
55. Costas A et al. Radial heterojunction based on single ZnO-CuxO core-shell nanowire for photodetector applications. *Sci. Rep*. 2019;91(9):1-9.
56. Zheng L, Hu K, Teng F, Fang X. Novel UV–visible photodetector in photovoltaic mode with fast response and ultrahigh photosensitivity employing Se/TiO_2 nanotubes heterojunction. *Small*. 2017;13:1602448-1602458.
57. Zheng L, Teng F, Zhang Z, Zhao B, Fang X. Large scale, highly efficient and self-powered UV photodetectors enabled by all-solid-state n-TiO_2 nanowell/p-NiO mesoporous nanosheet heterojunctions. *J Mater Chem C*. 2016;4:10032-10039.
58. Kalra A, Vura S, Rathkanthiwar S, Muralidharan R, Raghavan S, Nath DN. Demonstration of high-responsivity epitaxial β-Ga2O3/GaN metal-heterojunction-metal broadband UV-A/UV-C detector. *Appl Phys Express*. 2018;11:064101.
59. Liu K, Sakurai M, Liao M, Aono M. Giant improvement of the performance of ZnO nanowire photodetectors by Au nanoparticles. *J Phys Chem C*. 2010;114:19835-19839.
60. Kumar KDA et al. Insight into Al doping effect on photodetector performance of CdS and CdS:mg films prepared by self-controlled nebulizer spray technique. *J Alloys Compd*. 2021;892:160801. doi:10.1016/J.JALLCOM.2021.160801
61. Shuai M, Lingmin Y, Lei C, Chun L, Mingli Y, Xinhui F. Resistive-type UV–visible photodetector based on CdS NWs /ZnO nanowalls heterostructure fabricated using in-situ synthesis method. *J Alloys Compd*. 2020;827:154090.
62. Amiri M, Alizadeh N. Highly photosensitive near infrared photodetector based on polypyrrole nanoparticle incorporated with CdS quantum dots. *Mater Sci Semicond Process*. 2020;111:104964.
63. Huang G, Zhang P, Bai Z. Self-powered UV–visible photodetectors based on ZnO/graphene/CdS/electrolyte heterojunctions. *J Alloys Compd*. 2019;776:346-352.
64. Hussain AA, Sharma B, Barman T, Pal AR. Self-powered broadband photodetector using plasmonic titanium nitride. *ACS Appl Mater Interfaces*. 2016;8:4258-4265.
65. Hussain AA, Pal AR, Patil DS. An efficient fast response and high-gain solar-blind flexible ultraviolet photodetector employing hybrid geometry. *Appl Phys Lett*. 2014;104:193301.
66. Podder S, Pal AR. Plasmonic visible-NIR photodetector based on hot electrons extracted from nanostructured titanium nitride. *J Appl Phys*. 2019;126:083108.
67. Xiao H, Liang T, Xu M. Growth of Ultraflat PbI2 nanoflakes by solvent evaporation suppression for high-performance UV photodetectors. *Small*. 2019;15:1901767.

How to cite this article: Hadia NMA, Shaban M, Mohamed SH, et al. Highly crystalline hexagonal PbI_2 sheets on polyaniline/antimony tin oxide surface as a novel and highly efficient photodetector in UV, Vis, and near IR regions. *Polym Adv Technol*. 2022;1-11. doi:10.1002/pat.5829